Supplementary Information for: Giant energy storage ultrafast microsupercapacitors via negative capacitance superlattices

Suraj S. Cheema,[1*†] Nirmaan Shanker,[1†] Shang-Lin Hsu,[1†] Joseph Schaadt,[1,2] Nathan M. Ellis,[1] Matthew Cook,[3] Ravi Rastogi,[3] Robert C.N. Pilawa-Podgurski,[1] Jim Ciston,[4] Mohamed Mohamed,[3] Sayeef Salahuddin[1,5*]

[1] *Department of Electrical Engineering and Computer Sciences, University of California, Berkeley, CA, USA.*

[2] *Department of Mechanical Engineering, University of California, Berkeley, CA, USA.*

[3] *Lincoln Laboratory, Massachusetts Institute of Technology, Lexington, MA, USA.*

[4] *National Center for Electron Microscopy Facility, Molecular Foundry, Lawrence Berkeley National Laboratory, Berkeley, CA, USA.*

[5] *Materials Sciences Division, Lawrence Berkeley National Laboratory, Berkeley, CA, USA.*

[†] ***These authors contributed equally to this work.***

[*] ***Correspondence to: s.cheema@berkeley.edu (S.S.C), sayeef@berkeley.edu (S.S.)***

Supplementary Table 1. Benchmark to BEOL-compatible planar electrostatic capacitors. To restrict the literature to just those relevant for on-chip energy storage capacitors, only BEOL-compatible capacitors – namely ALD-grown dielectrics – are considered in this comparison table. Approaches to scale thickness without a multilayer approach[15] demonstrate degraded volumetric ESD, e.g. ZrO_2[18] and HZO[6,20]. *Note: Reference[12] examining Ta_2O_5-HZO employs a non-ALD (sputtered) dielectric layer. Furthermore, the loss due hysteresis is not reported in this work for both Ta_2O_5-HZO and Al_2O_3-HZO; therefore, one cannot directly compare recoverable ESD and efficiency. **Note: References[15] and[16] examining ZrO_2-TiO_2 multilayers employ non-CMOS-compatible Pt electrodes. Even considering some non-BEOL-compatible HfO_2- and ZrO_2-based results, this work still boast the largest volumetric ESD (at the $\sim$ 10 nm range) and largest areal ESD (due to persistence of AFE NC behavior to $\sim$ 100 nm regime in HZO-Al_2O_3 superlattices) for potential BEOL-compatible dielectrics. Abbreviations: energy storage density (ESD); thickness (t); efficiency (Eff); dielectric (DE); antiferroelectric (AFE); ferroelectric (FE); superlattice (SL); negative capacitance (NC). The comparison data points in Fig. 2i are taken from BEOL-compatible MIM capacitor results, namely fluorite-structure HfO_2-ZrO_2-based antiferroelectrics[2–9,13–15,18,19,21,22], and thicker ALD-grown dielectric oxides[1].

Dielectric	t (nm)	Order	ESD (J/cm^3)/(μJ/cm^2)	Eff (%)	Ref.
Al_2O_3	5	DE	50 / 25	n/a	[1]
Al_2O_3-ZrO_2	15-15	DE	40 / 120	n/a	[1]
Al_2O_3-TiO_2	15-7.8	DE	60 / 137	n/a	[1]
Zr:HfO_2 (70%)	9	AFE	46 / 41	52	[2]
Si:HfO_2 (5.6%)	9	AFE	40 / 36	80	[3]
ZrO_2	12	AFE	37 / 44	51	[4]
Si:HfO_2	10	AFE	61 / 61	65	[5]
Zr:HfO_2 (50%)	5.8	AFE	46 / 27	59	[6]
Zr:HfO_2 (50%)	7.1	AFE	55 / 39	57	[6]
Zr:HfO_2 (50%)	8.8	AFE	45 / 40	50	[6]
Zr:HfO_2 (50%)	10.2	AFE	44 / 45	51	[6]
Zr:HfO_2 (50%)	10.0	AFE	43 / 43	62	[6]
Zr:HfO_2 (50%)	20.2	AFE	42 / 85	62	[6]
Zr:HfO_2 (50%)	30	AFE	41 / 123	64	[6]
Zr:HfO_2 (50%)	40	AFE	34 / 136	63	[6]
Zr:HfO_2 (70%)	8	AFE	47 / 38	46	[6]
Zr:HfO_2 (70%)	9.2	AFE	46 / 42	48	[6]
Zr:HfO_2 (70%)	12	AFE	32 / 38	36	[6]
Zr:HfO_2 (70%)	19.0	AFE	21 / 40	42	[6]
Zr:HfO_2 (70%)	29.0	AFE	24 / 70	45	[6]
Al:HfO_2 (5.7%)	10	FE-AFE	33 / 33	45	[7]
Al:HfO_2 (6.9%)	10	AFE	42 / 42	58	[7]
Al:HfO_2 (8.8%)	10	DE	33 / 33	90	[7]
Al:HZO	10	AFE	52 / 52	80	[8]
Si:HZO	10	AFE	53 / 53	82	[8]
La:HZO	10	AFE	50 / 50	70	[9]
HfO_2	10	FE	10.6 / 10.6	91	[10]
Zr:HfO_2 (25%)	10	FE	14.6 / 14.6	90	[10]
Zr:HfO_2 (50%)	10	FE-AFE	20.2 / 20.2	78	[10]
Zr:HfO_2 (75%)	10	AFE	34 / 34	49	[10]
ZrO_2	10	AFE	37.6 / 37.6	58	[10]
Si:HfO_2 (5.8%)	10	AFE	40 / 40	75	[11]
Al_2O_3-Zr:HfO_2	4-7.7	NC DE-FE	n/a / n/a	n/a	[12]*
Ta_2O_5-Zr:HfO_2	13.5-11.5	NC DE-FE	n/a / n/a	n/a	[12]*
ZrO_2-HfO_2:Al_2O_3	5-2	FE-DE	54 / 38	51	[13]
Zr:HfO_2-Al_2O_3-Zr:HfO_2	10	AFE-DE-AFE	70 / 70	50	[14]
ZrO_2	8.7	AFE	94 / 82	80	[15]
TiO_2-ZrO_2-TiO_2	8.7	DE-AFE-DE	94 / 82	81	[15]**
TiO_2-ZrO_2 SL	48	DE-AFE	80 / 384	82	[15]**
TiO_2-ZrO_2-TiO_2	1-6-1	DE-AFE-DE	114.5 / 92	76	[16]**
Al:HfO_2	6.5	AFE	64 / 42	64	[17]
ZrO_2	4.3	AFE	45 / 19	60	[18]
ZrO_2	5.3	AFE	58 / 31	40	[18]
ZrO_2	6.5	AFE	48 / 31	53	[18]
ZrO_2	10.6	AFE	22 / 23	48	[18]
ZrO_2	14.7	AFE	18 / 26	44	[18]
HfO_2-ZrO_2	8.8	AFE	50 / 44	55-62	[19]
Zr:HfO_2 (70%)	5	AFE	22 / 11	75	[20]
Zr:HfO_2 (70%)	6	AFE	35 / 21	67	[20]
Zr:HfO_2 (70%)	7	AFE	32 / 22	66	[20]
Zr:HfO_2 (70%)	8	AFE	42 / 34	45	[20]
Zr:HfO_2 (70%)	10	AFE	30 / 30	39	[20]
Zr:HfO_2 (80%)	9	NC AFE	115 / 104	83	this work
Zr:HfO_2-Al_2O_3 SL	94	NC AFE-DE	81 / 761	73	this work

Supplementary Table 2. Benchmark to electrostatic microcapacitors. Electrostatic microsupercapacitors in various 3D geometries are considered. In this table, areal power density (W/cm^2) is defined by the reported areal ESD (J/cm^2) multiplied by the frequency of the measurement (capacitance-frequency impedance measurements in the case of normal dielectrics or *P*-*V* loops in the case of antiferroelectrics). For this work, areal power density is extracted from discharge measurements (Extended Data Fig. 9). Works on Si trenches reporting lower ESD than those listed in the table are not included. Abbreviations: areal energy storage density (E_A); frequency (f); areal power density (P_A); superlattice (SL); dielectric (DE); ferroelectric (FE); antiferroelectric (AFE); negative capacitance (NC); anodized aluminum oxide (AAO); carbon nanotubes (CNT); thickness (t).

Geometry	Dielectric	t (nm)	Order	Method	E_A (J/cm^2)	f (Hz)	P_A (W/cm^2)	Ref.
Nanowire	Cu_2O	30-50	DE	$1/2CV^2$	1.75e-3	1e6	1.75e3	[23]
Nanowire	Cu_2O	30-50	DE	$1/2CV^2$	1.25e-3	1e6	1.25e3	[23]
Nanowire	Cu_2O	30-50	DE	$1/2CV^2$	1.125e-3	1e6	1.125e3	[23]
Nanowire	Cu_2O	30-50	DE	$1/2CV^2$	6.25e-4	1e6	6.25e2	[23]
Nanowire	Cu_2O	30-50	DE	$1/2CV^2$	5.0e-4	1e6	5.0e2	[23]
Nanowire	Cu_2O	30-50	DE	$1/2CV^2$	3.75e-4	1e6	3.75e2	[23]
Self-rolled	Al_2O_3	6.7	DE	$1/2CV^2$	2.81e-5	1e3	2.81e-2	[24]
Self-rolled	Al_2O_3-HfO_2-TiO_2	7	DE	$1/2CV^2$	2.02e-5	1e3	2.02e-2	[25]
AAO	Al_2O_3	6.7	DE	$1/2CV^2$	4.75e-4	20	9.50e-3	[26]
AAO	Al_2O_3	6.7	DE	$1/2CV^2$	8.8e-5	20	1.76e-3	[26]
AAO	Al_2O_3	8	DE	$1/2CV^2$	3.71e-4	20	7.42e-3	[27]
AAO	Al_2O_3	8	DE	$1/2CV^2$	6.59e-4	20	1.32e-2	[27]
AAO	Al_2O_3	8	DE	$1/2CV^2$	8.38e-4	20	1.68e-2	[27]
AAO+CNT	Al_2O_3	10	DE	$1/2CV^2$	8.67e-3	1e2	8.67e-1	[28]
Si trench	Al_2O_3	10	DE	$1/2CV^2$	7.92e-4	1e4	7.92	[29]
Si trench	SiO_2-Si_3N_4	15	DE	$1/2CV^2$	2.24e-3	1e5	2.24e2	[30]
Si trench	Al_2O_3	55	DE	$1/2CV^2$	1.23e-3	1e3	1.23	[31]
Si trench	$HfAlO_x$	40	DE	$1/2CV^2$	6.12e-3	n/a	5.66e2	[32]
Si trench	ZrO_2-Al_2O_3-ZrO_2	7.5	AFE	$\int V \cdot dP$	6.98e-4	1e5	6.98e2	[4]
Si trench	Si:HfO_2	10	AFE	$\int V \cdot dP$	4.5e-4	1e2	4.5e-2	[11]
Si trench	Si:HfO_2	10	AFE	$\int V \cdot dP$	4.06e-4	1e3	4.06e-1	[33]
Si trench	Si:HfO_2-Al_2O_3-Si:HfO_2	20	AFE	$\int V \cdot dP$	7.18e-4	1e3	7.18e-1	[33]
Si trench	HZO-Al_2O_3 SL	90	NC AFE	$\int V \cdot dQ$	8.00e-2	1e6	3.0e5	this work

Supplementary Table 3. Benchmark to electrochemical microsupercapacitors. The values in this table are taken from summary tables reporting both areal power density (W/cm^2) and areal ESD (J/cm^2) in the following recent reviews benchmarking state-of-the-art energy storage micro-capacitors[64,65]. The benchmark plot of electrochemical microsupercapacitors in Figure 3 considers activated carbon (AC)[34,55], onion-like carbon[34], carbide-derived carbon[35], graphene[63], AC and Zn-ion[36], RuO_2[57,58], which are detailed in this table. Works demonstrating below 10 mJ/cm^2 are not included in the table. For 3D electrochemical microsupercapacitors (as opposed to thin film microsupercapacitors), the 3D scaffold depth is provided (rather than the electrode thickness). Abbreviations: areal energy storage density (E_A); areal power density (P_A); activated carbon (AC); acetonitrile (AN); carbide-derived carbon (CDC); sodium carboxymethylcellulose (CMC); carbon nanotube (CNT); 1-ethyl-3-methylimidazolium tetrafluoroborate (EMI, BF_4); 1-ethyl-3-methylimidazolium (EMIM); 1-ethyl-3-methylimidazolium bis(trifluoromethylsulfonyl)imide (EMIM, TFSI); graphene and vanadium nitride quantum dots (G–VNQD); layer double hydroxides (LDH); laser-scribed graphene (LSG); multiwall carbon nanotubes (MWCNT); nanowires (NW); onion-like carbon (OLC); polyanline (PANI); propylene carbonate (PC); poly(3,4-ethylenedioxythiophene) (PEDOT); poly(pyrrole) (PPy); poly(vinyl alcohol) (PVA); thickness/depth (t/d).

Electrode	t/d (μm)	Electrolyte	Potential (V)	E_A (mJ/cm^2)	P_A (mW/cm^2)	Ref.
AC	5	1M Et_4NBF_4 in PC	3.0	12	20	34
CDC	4.1	2M EMI, BF_4 in AN	3.0	54	30	35
Zn nanosheet / AC	50/80	$ZnSO_4$/CMC	1.5	415	0.16	36
Ti_3C_2 / Co-Al-LDH	n/a	6M KOH	0.4-1.45	39	8.8	37
AC	2	1M NEt_4-BF_4 in PC	2.5	26	44.9	38
MWCNT / MnO_2	0.5 / 0.6	0.5 M Na_2SO_4	1.8	16	675	39
TiC-CDC	4.1	2M EMIM-BF_4 in AN	3V	311	100	35
TiC-CDC	3.2	1M H_2SO_4	0.9	42	100	40
VN	3.4	1M KOH	0.6	40	10	41
OLC	7	ionic liquid	3.7	30	240	42
Graphene	7.6	iongel	2.5	22	152	?
TiC-CDC	7	2M EMIM-BF_4 in ACN	3	324	5.3	43
Graphene-FeOOH / graphene-MnO_2	41	PVA LiCL	1.8	143	11.8	44
AC / MnO_2	10	0.2M K_2SO_4	1.5	135	7	45
Graphene / RuO_2	7.6	1M H_2SO_4	1	80	6	46
PANI nanowires	10.1	PVA H_2SO_4	1	73	4.5	47
Graphene-PANI	4.5	PVA H_2SO_4	1	163	4.5	48
AC	70	1M $NaNO_3$	1	180	51.5	49
V2O5 / G-VNQD	100	PVA LiCL	1.6	165	3.8	50
(3D) MnO_2 / MnO_2 in Si microtubes	68/68	0.5M Na_2SO_4	0.8	36	20	51
(3D) MnO_2 in Si NW	50	Ionic liquid	2.2	33	0.05	52
(3D) RuO_2 in Si-SiO_2-Ai pillars	10-80	0.1M Na_2SO_4	1.0	12	5	53
(3D) PPy in C rods	140	0.1M KCl	0.8	43	1	54
(3D) AC in etched cavities	215	1M Et_4NBF_4 in PC	2.5	257	34	55
(3D) AC in etched channels	90	1M $NaNO_3$	0.5	11	52	49
(3D) AC in SU-8 photoresist walls	250	PVA-based	0.8	43	1	56
(3D) RuO_2 in C nanowall	12	PVA-based	0.9	176	28	57
(3D) RuO_2 in porous Au	80	PVA-based	0.9	454	8	58
(3D) Ppy in 3D Si nanotrees	50	ionic liquid	1.5	15	0.8	59
(3D) MnO_2 & AC in Ni nanocone	2	iongel	2.5	2	0.3	60
(3D) PANI nanofiber in polymer microcavity	15	PVA H_2SO_4	0.8	21	3	61
(3D) Carbon in Si NWs	120	EMIM-TFSI	2.7	2	8	62
(3D) MnO_2 in Si micro-tubes	68	0.5M Na_2SO_4	0.8	13	20	51
(3D) Graphene & MnO_2 in 3D LSG	15	1M Na_2SO_4	0.9	162	1	63

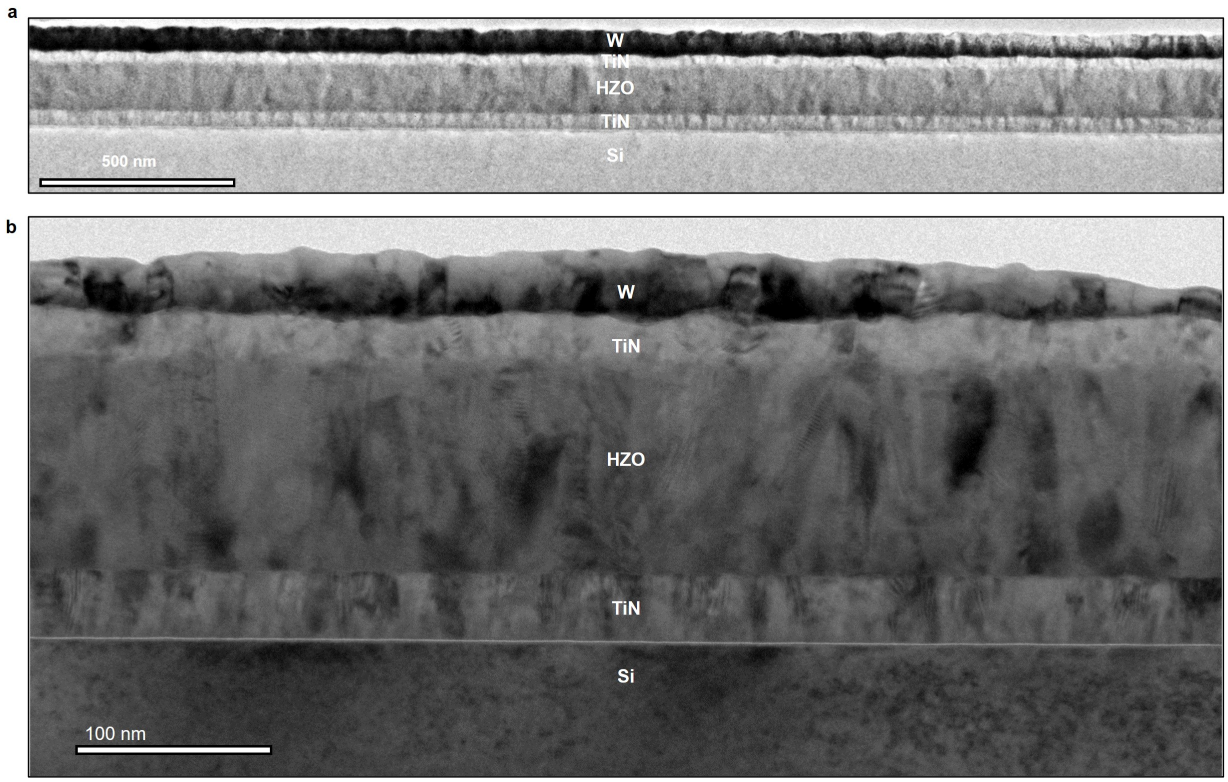

Supplementary Fig. 1. Wide field-of-view TEM image of HZOx10 continuous film. (**a**) Wide field-of-view TEM for the Si/TiN/HZOx10 continuous/TiN/W MIM structure. (**b**) Zoomed-in TEM demonstrating the presence of vertical columnar-like grains in the HZO layer; the constrained grain growth can help maintain the ferroelectric o-phase in the ultrathick regime (Extended Data Fig. 5).

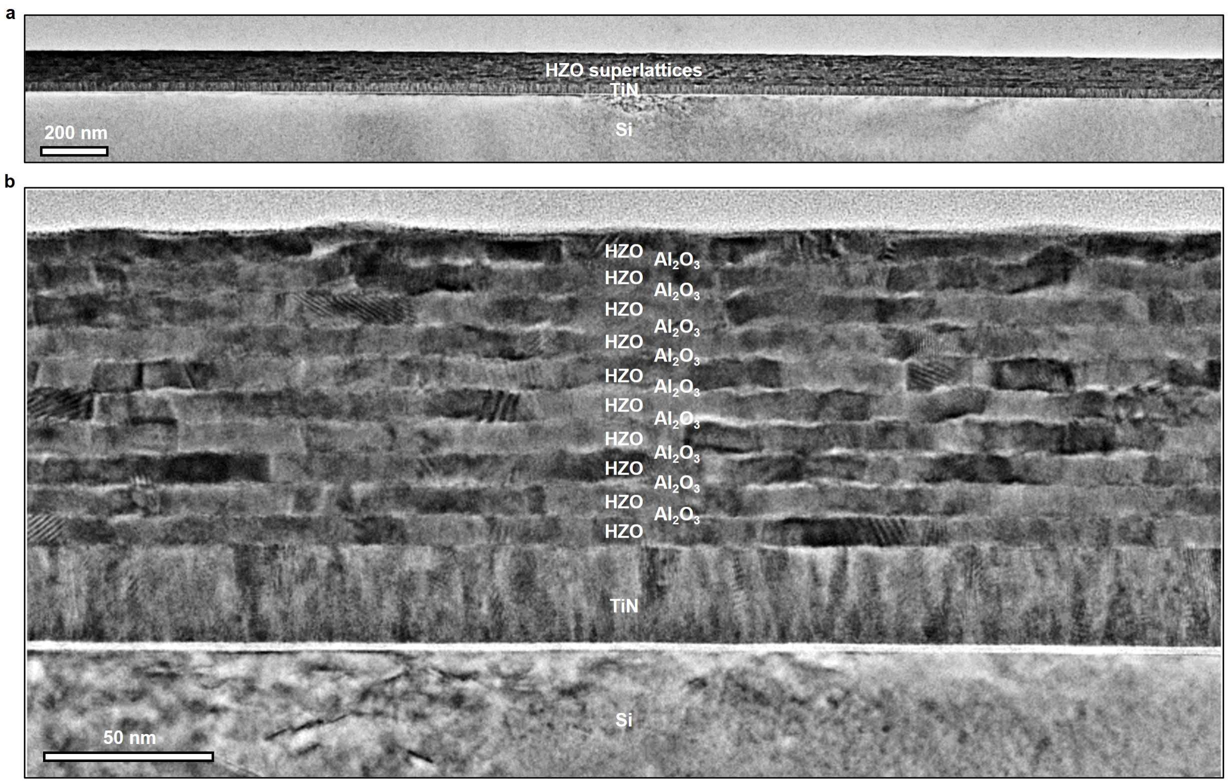

Supplementary Fig. 2. Wide field-of-view TEM image of HZOx10 superlattice film. (a) Wide field-of-view TEM for the HZOx10 superlattice (HZO-Al_2O_3 structure) grown on TiN-buffered Si. **(b)** Zoomed-in TEM demonstrating well-separated Al_2O_3 and HZO layers despite ultrathin (5 Å) Al_2O_3 interlayers, consistent with XRR analysis indicating 5 Å Al_2O_3 serves as a sufficient barrier layer (Extended Data Fig. 3). The wavy morphology in the superlattice likely derives from the polycrystalline nature of the HZO layers; the domains in various orientations result in a topology that varies over wide distances, although the films are atomically-smooth over small distances (Extended Data Fig. 3). As the ALD Al_2O_3 layers conformally coats the HZO surfaces, the rumpled morphology becomes more pronounced with increasing superlattice layers. Despite this topology, the conformal nature of ALD enables the t-phase to persist across the entire thickness, as identified from oxygen imaging analysis of various HZO superlattice layers (Fig. 2c, Extended Data Fig. 4).

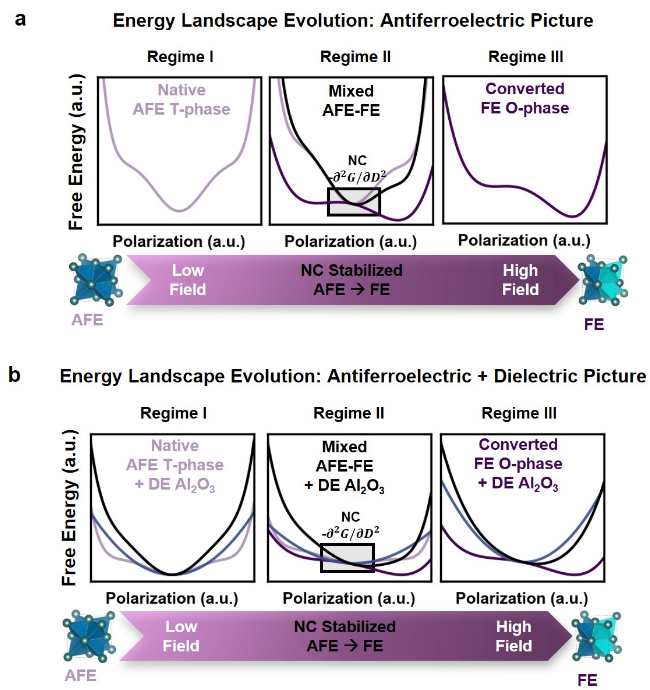

Supplementary Fig. 3. Energy landscape evolution for antiferroelectric and antiferroelectric-dielectric superlattices. **(a, b)** Energy landscape evolution of antiferroelectric HZO (a) and antiferroelectric-dielectric (HZO - Al_2O_3) superlattices (b) as the HZO transforms from the native antiferroelectric t-phase (left, Regime I) to mixed antiferroelectric-ferroelectric t-o phase (center, Regime II) to fully ferroelectric o-phase (right, Regime III) with increasing electric field. For the antiferroelectric picture (a), pink, purple, and black colors correspond to the t-phase, o-phase, and mixed t-o phase energy landscapes, respectively. For antiferroelectric HZO (a), the flattened energy landscape in Regime II due to antiferroelectric-ferroelectric phase competition (center) stabilizes NC and enhances permittivity, leading to the charge-boost behavior (Fig. 1). For the antiferroelectric-dielectric HZO-Al_2O_3 superlattices ((b), beyond the NC stabilization due to antiferroelectric-ferroelectric phase competition in the HZO layers, the additional dielectric Al_2O_3 layers (energy landscape in blue) can also help stabilize NC by depolarizing the ferroelectric phase fractions in Regimes II and III. The dielectric layers do not aid NC stabilization in steady-state (Regime I) as both dielectric Al_2O_3 and the native antiferroelectric t-phase have energy landscapes with only positive curvatures. This energy landscape picture is consistent with the observation of

NC (experimentally identified as negative curvature in hysteretic Q-E loops) for both antiferroelectric HZO (Fig. 1f) and antiferroelectric HZO-Al_2O_3 superlattices (Fig. 2g) only at intermediate fields (not low fields).

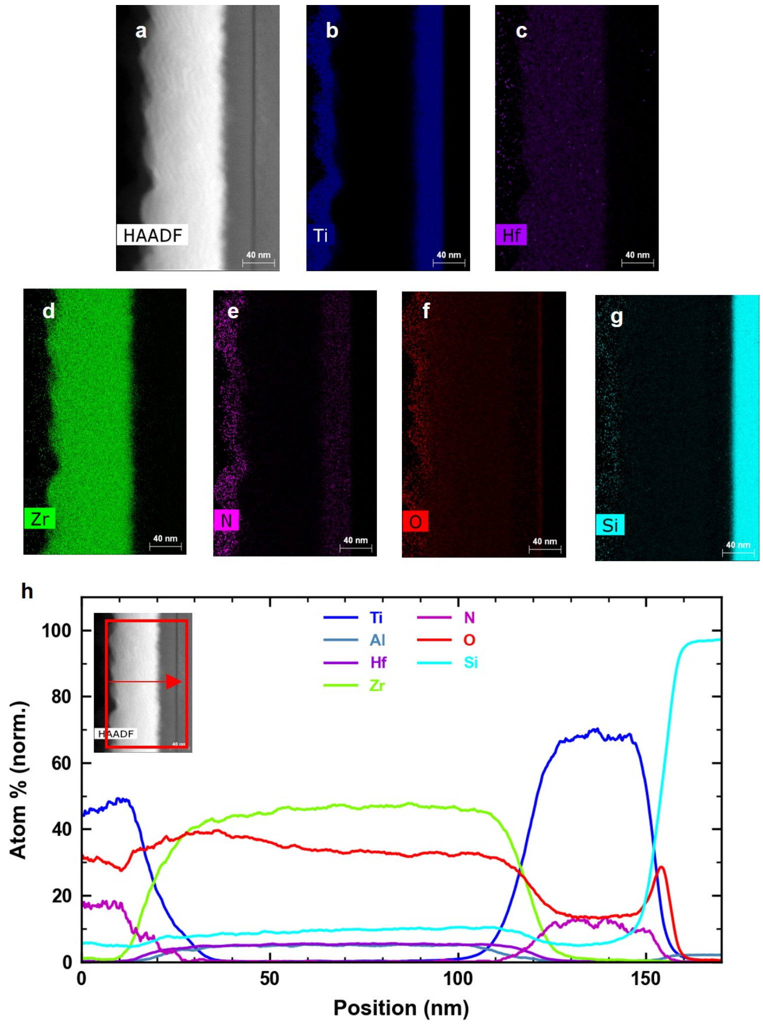

Supplementary Fig. 4. EDS of sidewall of 3D Si trench capacitor. **(a)** HAADF-STEM image of the TiN - HZOx10 superlattice (Al_2O_3-HZO) - TiN MIM structure deposited at the sidewall of the 3D Si trench capacitor. The superlattice Al_2O_3-HZO structure can be more clearly distinguished by eye based on the alternating light and dark regions in Fig. 3a. **(b-g)** Corresponding EDS elemental mapping of Ti (b), Hf (c), Zr (d), N (e), O (f) and Si (g). The relative atomic percentages of Hf and Zr match the expected 20:80 Hf:Zr composition in the HZO films, which indicates the composition profile is maintained in the superlattice structure and the trench. **(h)** Corresponding elemental profile as a function of position matching with the expected MIM structure.

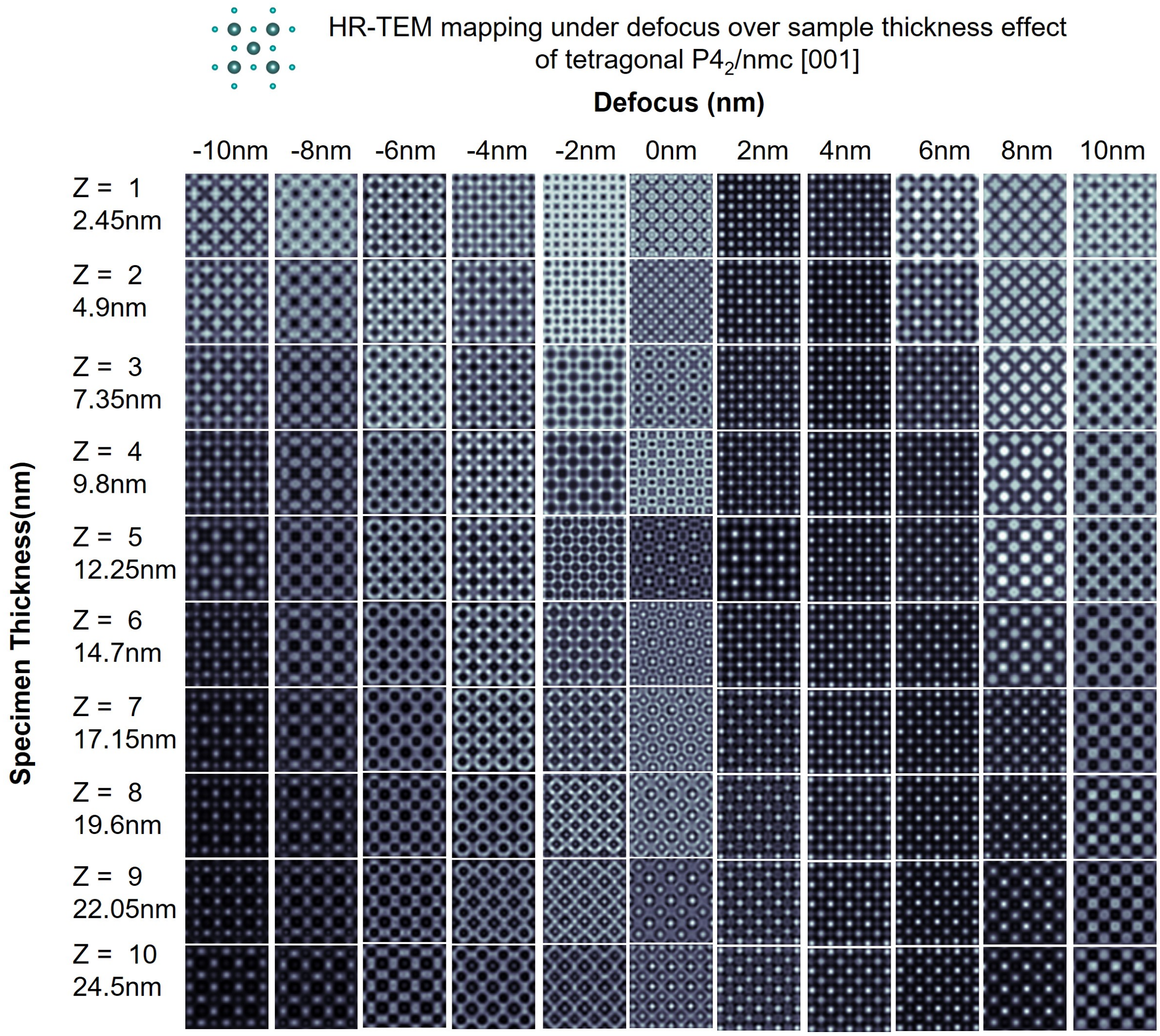

Supplementary Fig. 5. Determining oxygen imaging conditions from HR-TEM simulations. The simulation and experimental conditions used for t-phase analysis in HZOx10 superlattices (Extended Data Fig. 4) are provided in the Methods section. Further details on this analysis can be found in our previous work[66].

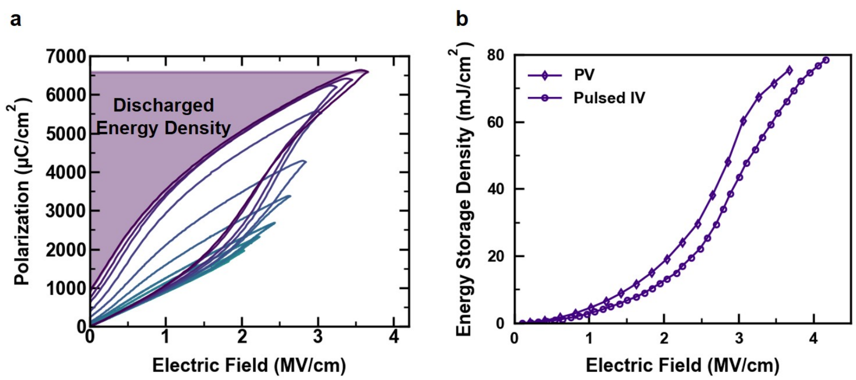

Supplementary Fig. 6. Comparison of ESD extracted from pulsed *I-V* measurements and conventional P-E measurements **(a)** Measured polarization-electric field (*P-E*) curves obtained from bipolar triangular waveforms at 10 kHz (Methods) for a HZOx10 superlattice trench capacitor. The ESD is calculated by $\int_{P_{rem}}^{P_{max}} EdQ$ (Methods), which is equivalent the purple shaded area. **(b)** Comparison of ESD extracted from pulsed *I-V* and conventional *P-V* measurements for the same sample. The ESD extracted from *P-V* measurements is shifted slightly to the left as *P-V* measurements occur at substantially slower time scales (100 μs) compared to the 1.5 μs pulses applied in the pulsed *I-V* measurement, which allows for more charge to be stored at lower fields. Overall, both methods yield similar areal energy storage density values.

Supplementary text

Thickness scaling considerations

Scaling up fluorite-structure antiferroelectricity Fluorite-structure superlattices is an emerging engineering strategy[67] for enhanced ferroelectric performance, particularly for computing applications[68–72]. Here, we look to employ fluorite-structure superlattices for enhanced performance in energy storage, namely scaling up the total energy density.

Increasing the net energy stored requires increasing the film thickness while maintaining the antiferroelectric negative capacitance behavior. This is an issue for fluorite-structure (anti)ferroelectrics, since their critical thickness is limited to the 10-nm regime[73]. The first case of Al_2O_3 interlayers showed it can effectively control the HZO grain size and thereby maintain the stability range for HZO ferroelectricity to 40 nm thickness[74]. Later attempts to increase fluorite-structure ferroelectricity got up to the 50-nm regime using nanolaminates with Al_2O_3[75–77]. And more recent works examined the effect of Al_2O_3 interlayers on the ferroelectric microstructure[78,79].

Scaling up the antiferroelectric thickness is more difficult than the ferroelectric thickness; the t-phase is stable for ultrasmall grain sizes in HZO[80] before it transforms to the o-phase and subsequently the m-phase with increasing grain size, which scales with film thickness[80]. Previous work on HZO thin films found increasing thickness monotonically increases (decreases) the amount of monoclinic (tetragonal) phase, particularly in the thick (20 nm and above) regime[81]. Antiferroelectricity has been scaled to 48 nm in TiO_2-ZrO_2 heterostructures[15] and 20 nm in Al_2O_3-Si:HfO_2 heterostructures[33] to improve total energy storage. Other attempts to increase the thickness beyond 100 nm did not employ conformal ALD[82–86], so they cannot be considered for scaled 3D-integrated devices.

In this work, through HZO(80% Zr)-Al_2O_3 superlattices, we demonstrate antiferroelectricity to 100 nm. The Al_2O_3 interlayers interrupt the continual growth of HZO films, and the resulting decrease of grain size prevented the formation of the monoclinic phase. Additionally, Zr-rich HZO is expected to be a better candidate for pushing t-phase stability to thicker regime considering the larger critical grain size for t-phase stability in ZrO_2[87,88] compared to HfO_2[89].

Breakdown strength thickness scaling Thick dielectric ceramic films are expected to have lower breakdown fields with increasing thickness[90,91], consistent with the drop in breakdown field in the thicker HZO-based films (Fig. 2) to the baseline 9 nm HZO films (Fig. 1). Now just focusing on the ultra-thick case (Fig. 2), we observe the HZO-Al_2O_3 superlattice films demonstrate higher breakdown strength compared to the continuous HZO films (Extended Data Fig. 8d). Various reasons can explain the higher breakdown strength in the superlattices compared to continuous ultra-thick HZO (Extended Data Fig. 8d), including (i) the presence of interfaces i.e. electrical tree effect, or (ii) incorporation of a larger breakdown field system, which should increase the overall breakdown field approximately according to a weighted volume fraction in a Vegard's law-like manner, or (iii) finer grain size, which should increase the volume fraction of high-resistivity grain boundaries[92]. All of the above mechanisms are consistent with the significantly lower leakage current present in the superlattices (Extended Data Fig. 8a), consistent with previous reports on HZO-based superlattices with very thin Al_2O_3 interlayers[93,94].

Therefore, it is likely the finer grain size via the amorphous layer templating not only maintains the desirable antiferroelectric structure (Fig. 2), but also helps increase the breakdown field, thereby improving both charge and voltage ingredients that contribute to electrostatic energy storage.

Negative capacitance energy storage considerations

Ferroic phase transitions Regime II demonstrating NC coincides with the uptick in permittivity, charge storage, and the field-driven nonpolar-to-polar phase transition (t-o phase coexistence) (Fig. 1), underlying the role of NC in these macroscopic quantities and microscopic phenomena. Indeed, one origin of NC in ferroelectric materials stems from the stored energy of a phase transition; NC effects were previously transiently measured during the switching of a ferroelectric capacitor[95]. Here, instead of a ferroelectric polarization switch, the mechanism of NC is due to the field-driven ferroelectric transition in antiferroelectric HZO, which gives rise to enhanced charge storage. Proximity to ferroelectric phase transitions have been identified as the key microscopic origin of NC in seminal works on perovskites[96] and fluorites[68]. We experimentally find this antiferroelectric phase transition is inextricably linked to the NC effect (Fig. 1), as has been recently demonstrated in fluorite-structure antiferroelectric ZrO_2[97] and canonical perovskite-structure antiferroelectric $PbZrO_3$[98]. Therefore, the NC effect and field-driven ferroelectric transition are intimately tied, and the associate charge-boost from such phenomena may be a generic feature across a wide class of antiferroelectrics. However, this antiferroelectric mechanism of NC had yet to be leveraged to enhance charge storage in energy storage capacitors before this work.

Due to the different nature of the forward (t-to-o, nonpolar-to-polar) and reverse (o-to-t, polar-to-nonpolar) phase transitions associated with antiferroelectricity, charging (forward) and discharging (reverse) branches of pulsed hysteretic charge-voltage measurements may not demonstrate the same degree of NC (manifested as a negative *dQ/dE* slope). For example, the HZOx10 superlattice in the 3D trench capacitor structure does not demonstrate as clear behavior in the discharging branch as it does in the charging branch (Fig. 3e inset), while, the HZOx10 superlattice in the 2D planar capacitor structure does demonstrate clear NC behavior in both charging and discharging loops (Fig. 2g). This indicates if the antiferroelectric phase stabilization and NC behavior in the 3D trench capacitor can be further optimized (as it is in the 2D planar capacitors) during the discharge branch, an even larger recoverable energy storage can be achieved, due to diminished hysteresis loss. Also, note the negative slope from hysteretic$Q$-V measurements during the discharge branch will become more pronounced if the charge contribution from the dielectric portion of the superlattice (Al_2O_3) were subtracted away to leave behind just the HZO portion, as is done in typical NC analysis to isolate the NC effect in the ferroic component[68]. In this work, this analysis is not performed to simply report the Q-V data and enhanced energy storage corresponding to the superlattice as a whole, as the NC behavior is evident even without the dielectric component subtraction.

Overcoming breakdown-permittivity trade-off Enhanced charge storage via the NC effect sets a paradigm of new materials design for electrostatic capacitors by overcoming a fundamental material properties trade-off: dielectric permittivity (κ) versus breakdown strength (E_{BD}) (Extended Data Fig. 10). In particular, dielectric materials tend to follow an empirical κ-E_{BD} trend[92], in which an approximate $E_{BD} \sim k^{-1/2}$ relation exists empirically over a very wide-range of dielectric materials (over nearly 2–3 decades of dielectric constant)[92], explained by thermochemical breakdown models[99–101]. This is a critical relationship for ESD materials design since energy density can be approximately expressed as proportional to the permittivity of the dielectric and the square of the applied electric field[92]. Note this relation assumes a linear dielectric with a permittivity that is independent of the electric field, although dielectric permittivities usually exhibits nonlinearity under very high electric field; nonetheless, most dielectric materials tend to follow the general κ-E_{BD} trend[92] which prevents breakthrough ESD values. Therefore, strategies to enhance energy storage in dielectrics generally follow one of two strategies[92]: improving breakdown strength in high dielectric constant systems, e.g. via defect engineering in relaxor ferroelectrics[102], or improving dielectric constant in high breakdown strength systems, e.g. via antiferroelectric NC as in this work.

Overcoming speed-capacity trade-off The antiferroelectric order and its associated field-driven phase transition is especially key for energy storage. In particular, the NC phenomena stabilized at intermediate fields within the bulk of the antiferroelectric material opens access a second "super-linear" electrostatic regime (Regime II) contributing to higher charge storage, which is not present in just any nonlinear dielectric, e.g. conventional ferroelectric materials (Fig. 1). In that sense, this antiferroelectric NC approach can be considered as an electrostatic analog to electrochemical pseduocapacitors (PCs)[103], which leverage additional chemical reaction charges via surface redox reactions, in addition to physical surface charges, like standard electrochemical electric double layer capacitors (EDLCs). Here, the charge-boosting NC ferroic phase transitions serve as structural analogs to the charge-boosting chemical reactions that enhance energy storage in electrochemical PCs. However, unlike relying on slow chemical reactions like PCs which reduce power density relative to EDLCs[103], ferroic phase transitions do not slow down the energy storage operation. Therefore, the NC effect at ferroic phase transitions can foster enhanced charge storage without sacrificing speed. Accordingly, the 3D-integrated NC superlattices simultaneously demonstrate record energy density and power density across all electrostatic systems and overcome the traditional speed-capacity trade-off across the energy storage hierarchy (Fig. 3b).

On-chip energy storage considerations

Benchmarks: BEOL Capacitors Supplementary Table 1 benchmarks the areal energy storage density for ALD-grown dielectric electrostatic capacitors, including Al_2O_3-based dielectrics, ZrO_2 antiferroelectrics, and doped-HfO_2 (anti)ferroelectrics, including Zr:HfO_2, Si:HfO_2, Al:HfO_2, and La:HfO_2. Directionally-grown dielectrics (e.g. perovskites) are not shown in this comparison since they currently cannot be conformally grown into such 3D structures and therefore are not as relevant for on-chip area-confined application spaces, in which energy storage per area is the most relevant metrics; therefore, only conformally-grown dielectrics via ALD are considered. In our simple binary oxides grown by ALD, (anti)ferroelectric order and the corresponding enhanced energy storage behavior can be stabilized at low thermal budget, in particular below the 400°C requirement for back-end-of-the-line (BEOL) compatibility, consistent with previous work on ALD-grown HfO_2-ZrO_2 films on silicon[80,104].

Benchmarks: Microcapacitors Supplementary Table 2 benchmarks dielectric electrostatic capacitors in 3D-integrated structures, including anodized aluminum oxide (AAO)[26–28,105,106], self-rolled structures[24,25], and Si pores and trenches[29–32,107]. Recently, even antiferroelectric ZrO_2-based dielectrics have been integrated into Si trenches[4,11,33]. Relevant energy storage values are reported normalized to per square centimeter considering capacitance-, power- and energy-density per footprint area are more important indicators than volumetric or gravimetric metrics for practical miniaturized devices due to the limited integration area into ultrasmall systems[64,108]. Notably, nanostructured storage devices[109] with 3D metal-insulator-metal (MIM) architectures – spanning ALD-filled porous Si templates[110], ALD-filled anodic aluminium oxide (AAO) self-assembled templates[26], self-assembled rolled metallic structures[24], and ALD-filled trenched nanostructures (the modern VLSI technique)[29] – have successfully increased capacitance density, and therefore energy stored, per unit planar area[111] to help significantly reduce footprint and aid in integration. These templates require deposition techniques capable of conformal metal and insulator deposition inside the porous nanostructures, namely ALD. Additionally, HfO_2-based ferroelectric thin films have been vertically integrated into 3D trenches to amplify the polarization per footprint for nonvolatile memory applications[112] and ZrO_2-based antiferroelectric thin films were later demonstrated in DRAM capacitors[4].

Supplementary Table 3 benchmarks ESD and PD values for electrochemical microsupercapacitors taken from tabulated values listed in reviews on microsupercapacitors[64,65]. The values plotted in the benchmark Ragone plot (Fig. 3b) are from these works. This benchmark figure also considers commercial solid-state thin film Li microbatteries[113]. Again, relevant energy storage and power metrics are reported normalized to per footprint area (square centimeter) considering this work's focus on miniaturized energy storage devices for electronic microsystems[64,108].

3D geometries and dielectric behavior *C-V* results indicate the antiferroelectric behavior is maintained for the Al_2O_3-HZO superlattice in the 3D trench capacitor (Fig. 3d), which is not a trivial assumption due to the complications introduced from 3D deposition[11,33,114]. For example, stresses and composition variations from trench deposition may affect ferroic phase stabilization, as previously observed in Si:HfO_2[11,33]. One possible explanation is the HfO_2-ZrO_2 ferroic phase space is not as sensitive to composition variations as Si:HfO_2[73], as the HZO system has a much wider composition range for (anti)ferroelectric stabilization. If there were slight variations in ferroic phase stabilization derived from the nature of 3D deposition, the ESD boost in the trench may exhibit increased hysteresis loss from non-ideal ferroic phase fractions and/or inhomogeneities, which would diminish the recoverable ESD.

Regarding reliability, the HZOx10 superlattice in 3D trench capacitors breakdown at lower applied electric fields than the HZOx10 superlattice in 2D planar capacitors. One potential explanation is the trench capacitors suffer from more surface inhomogeneities e.g. pores, uneven and rougher surface (caused by the etching process), and bends; local electric fields around these non-ideal regions can exceed the applied electric field, thereby compromising the dielectric breakdown strength[92]. Lower breakdown fields have also been previously reported in trench capacitor structures and anodized aluminum oxide (AAO) nanocapacitors. For example, Al_2O_3-based MIM structures in AAO nanostructures report breakdown fields below 5 MV/cm[26], much below the expected value for Al_2O_3; passivisation techniques can help improve the breakdown field[27], which has been shown to significantly improve the energy density[27].

3D geometries and integration considerations Integrating electrostatic capacitors into trenches has advantages to other 3D electrostatic structures (Fig. 3b), specifically regarding scaling up areal ESD. Alternative 3D geometries – such as bottom-up self-assembled nanopores based on anodized aluminum oxide (AAO) and top-down self-assembled nanocapacitor structures via rolled-up technologies – are limited by their nanopore diameter and dense windings respectively, which both greatly limits the dielectric thickness and thereby limits scaling of the total amount of energy stored per footprint (Fig. 3b). This leaves trench structures conformally coated by ALD MIM layers, which has no such thickness limitations considering the trench width can be on the micron-scale (Fig. 3b).

Electrochemical microsupercapacitors and microbatteries This 3D electrostatic strategy also offers distinct on-chip microelectronics integration benefits compared to miniaturized electrochemical energy storage units. Electrochemical microsupercapacitors are considered promising for on-chip energy storage due to faster charge/discharge capability, i.e. higher power density, than their microbattery counterparts, stemming from different charge storage mechanisms, namely surface-mediated ion diffusion as opposed to bulk redox reactions. Still, electrochemical microsupercapacitors are many orders of magnitude lower in power density than the electrostatic microcapacitors reported here (Fig. 3b), due to the inherently faster mechanism of electrostatic charging/discharging. Beyond slow charge/discharge rates, both electrochemical microsupercapacitors and microbatteries face challenges due to poor technological readiness[115,116] derived from robustness of operation[64,103], low operation voltage, reliance on advanced 2D microelectrode materials (e.g. MXenes, carbon nanotubes, graphene)[117], packaging complexities (e.g. multi-component systems of collectors, electrolytes, separators, binders, connectors, electrodes)[108], complex microfabrication incompatible with silicon-based electronics (e.g. hydrothermal lithiation, laser structure patterning, 3D printing, template-assisted methods)[64], among other concerns, all of which prevent the realization of Si-integrated on-chip energy storage units[118].

To improve integration compatibility and safety concerns affiliated with miniaturized electrochemical energy storage systems, all solid-state thin-film lithium-ion microbatteries have recently garnered significant interest[119,120]. However, improvements in key performance metrics – e.g. ionic conductivity, energy density, specific power, energy efficiency, energy retention, cycling stability – and manufacturing still remain before full-scale realization[116,121–126].

In stark contrast, the 3D electrostatic microsupercapacitors reported here involve both BEOL-compatible materials – ALD-grown HZO – and standard very-large-scale-integration (VLSI) microfabrication processes – Si-etched trenches – used into today's state-of-the-art microelectronics.

On-chip microsupercapacitor applications These integrated microsupercapacitors are ideal partners to work in tandem with on-chip energy harvesting units, e.g. for self-powered autonomous on-chip nanosystems[64,118] and microelectronics waste heat recovery via pyroelectricity. Indeed, BEOL pyroelectric energy harvesting in the same HZO thin film system has been recently demonstrated[127]. And just as the total energy harvested via pyroelectricity has been recently scaled up in oxide ferroelectrics[128], a corresponding scale-up for energy storage will be required, as the first steps were taken here. Furthermore, fluorite-structure binary oxides based on CeO_2-Gd_2O_3 have recently reported record piezoelectric and electrostrictive response[129,130] relevant for electromechanical energy harvesting; this, in tandem with the record electrostatic energy storage reported here in the HfO_2-ZrO_2 family, offer promise for co-integrated self-powered energy microsystems based on simple fluorite-structure binary oxides.

Besides providing ideal on-chip power sources for Internet-of-Things-enabled microelectronic devices[64,115,118,131], artificial intelligence agents[132], and microrobotics[133–135], these microsupercapacitors can serve as ultrafast batteries for mobile devices, ultrafast power delivery sources for display applications, and ultrafast battery backups for volatile memory units, e.g. SRAM and DRAM. In addition, high density capacitors may contribute to the dramatic miniaturization and full integration of switched mode power supplies, whose volume is largely comprised of energy storage elements[136].

1. Spahr, H. *et al.* Enhancement of the maximum energy density in atomic layer deposited oxide based thin film capacitors. *Applied Physics Letters* **103**, 042907 (2013).

2. Park, M. H. *et al.* Thin $Hf_xZr_{1-x}O_2$ Films: A New Lead-Free System for Electrostatic Supercapacitors with Large Energy Storage Density and Robust Thermal Stability. *Advanced Energy Materials* **4**, 1400610 (2014).

3. Hoffmann, M. *et al.* Ferroelectric phase transitions in nanoscale HfO_2 films enable giant pyroelectric energy conversion and highly efficient supercapacitors. *Nano Energy* **18**, 154–164 (2015).

4. Pešić, M., Hoffmann, M., Richter, C., Mikolajick, T. & Schroeder, U. Nonvolatile Random Access Memory and Energy Storage Based on Antiferroelectric Like Hysteresis in ZrO_2. *Advanced Functional Materials* **26**, 7486–7494 (2016).

5. Ali, F. *et al.* Silicon-doped hafnium oxide anti-ferroelectric thin films for energy storage. *Journal of Applied Physics* **122**, 144105 (2017).

6. Kim, K. D. *et al.* Scale-up and optimization of HfO_2-ZrO_2 solid solution thin films for the electrostatic supercapacitors. *Nano Energy* **39**, 390–399 (2017).

7. Park, M. H. *et al.* Effect of acceptor doping on phase transitions of HfO_2 thin films for energy-related applications. *Nano Energy* **36**, 381–389 (2017).

8. Lomenzo, P. D., Chung, C.-C., Zhou, C., Jones, J. L. & Nishida, T. Doped $Hf_{0.5}Zr_{0.5}O_2$ for high efficiency integrated supercapacitors. *Applied Physics Letters* **110**, 232904 (2017).

9. Kozodaev, M. G. *et al.* La-doped $Hf_{0.5}Zr_{0.5}O_2$ thin films for high-efficiency electrostatic supercapacitors. *Applied Physics Letters* **113**, 123902 (2018).

10. Kim, S. J. *et al.* Stress-Induced Crystallization of Thin $Hf_{1\text{˘}x}Zr_xO_2$ Films: The Origin of Enhanced Energy Density with Minimized Energy Loss for Lead-Free Electrostatic Energy Storage Applications. *ACS Applied Materials & Interfaces* **11**, 5208–5214 (2019).

11. Kühnel, K., Czernohorsky, M., Mart, C. & Weinreich, W. High-density energy storage in Si-doped hafnium oxide thin films on area-enhanced substrates. *Journal of Vacuum Science & Technology B* **37**, 021401 (2019).

12. Hoffmann, M. *et al.* Negative Capacitance for Electrostatic Supercapacitors. *Advanced Energy Materials* **9**, 1901154 (2019).

13. Silva, J. P. B. *et al.* Energy storage performance of ferroelectric ZrO_2 film capacitors: effect of HfO_2:Al_2O_3 dielectric insert layer. *Journal of Materials Chemistry A* **8**, 14171–14177 (2020).

14. Das, D., Gaddam, V. & Jeon, S. Insertion of Dielectric Interlayer: A New Approach to Enhance Energy Storage in $Hf_xZr_{1-x}O_2$ Capacitors. *IEEE Electron Device Letters* **42**, 331–334 (2021).

15. Yi, S.-H., Lin, H.-C. & Chen, M.-J. Ultra-high energy storage density and scale-up of antiferroelectric TiO_2/ZrO_2/TiO_2 stacks for supercapacitors. *Journal of Materials Chemistry A* **9**, 9081–9091 (2021).

16. Yi, S.-H., Chan, Y.-C., Mo, C.-L., Lin, H.-C. & Chen, M.-J. Enhancement of Energy Storage for Electrostatic Supercapacitors through Built-in Electric Field Engineering. *Nano Energy* **99**, 107342 (2022).

17. Zhou, J. *et al.* A 6.5 nm thick anti-ferroelectric $HfAlO_x$ film for energy storage devices with a high density of 63.7 J cm 3. *Journal of Physics D: Applied Physics* **55**, 014003 (2022).

18. Lomenzo, P. D. *et al.* Harnessing Phase Transitions in Antiferroelectric ZrO_2 Using the Size Effect. *Adv. Electron. Mater.* **8**, 2100556 (2022).

19. Yang, K. *et al.* Energy conversion and storage using artificially induced antiferroelectricity in HfO_2/ZrO_2 nanolaminates. *Composites Part B: Engineering* **236**, 109824 (2022).

20. Chen, Y. *et al.* Flexible $Hf_xZr_{1-x}O_2$ thin films on polyimide for energy storage with high flexibility. *IEEE Electron Device Letters* **43**, 930–933 (2022).

21. Anju Balaraman, A. & Dutta, S. Inorganic dielectric materials for energy storage applications: a review. *Journal of Physics D: Applied Physics* **55**, 183002 (2022).

22. Payne, A. *et al.* Dielectric, energy storage, and loss study of antiferroelectric-like Al-doped HfO_2 thin films. *Applied Physics Letters* **117**, 221104 (2020).

23. Liu, Z. *et al.* Anomalous high capacitance in a coaxial single nanowire capacitor. *Nature Communications* **3**, 879 (2012).

24. Bof Bufon, C. C. *et al.* Self-assembled ultra-compact energy storage elements based on hybrid nanomembranes. *Nano Letters* **10**, 2506–2510 (2010).

25. Sharma, R. *et al.* Large-Area Rolled-Up Nanomembrane Capacitor Arrays for Electrostatic Energy Storage. *Advanced Energy Materials* **4**, 1301631 (2014).

26. Banerjee, P., Perez, I., Henn-Lecordier, L., Lee, S. B. & Rubloff, G. W. Nanotubular metal-insulator-metal capacitor arrays for energy storage. *Nature Nanotechnology* **4**, 292–296 (2009).

27. Haspert, L. C., Lee, S. B. & Rubloff, G. W. Nanoengineering Strategies for Metal–Insulator–Metal Electrostatic Nanocapacitors. *ACS Nano* **6**, 3528–3536 (2012).

28. Han, F. *et al.* Dielectric capacitors with three-dimensional nanoscale interdigital electrodes for energy storage. *Science Advances* **1**, 1–7 (2015).

29. Klootwijk, J. H. *et al.* Ultrahigh Capacitance Density for Multiple ALD-Grown MIM Capacitor Stacks in 3-D Silicon. *IEEE Electron Device Letters* **29**, 740–742 (2008).

30. Brunet, M. & Kleimann, P. High-Density 3-D Capacitors for Power Systems On-Chip: Evaluation of a Technology Based on Silicon Submicrometer Pore Arrays Formed by Electrochemical Etching. *IEEE Transactions on Power Electronics* **28**, 4440–4448 (2013).

31. Mu, J., Chou, X., Ma, Z., He, J. & Xiong, J. High-Performance MIM Capacitors for a Secondary Power Supply Application. *Micromachines* **9**, 69 (2018).

32. Strambini, L. *et al.* Three-dimensional silicon-integrated capacitor with unprecedented areal capacitance for on-chip energy storage. *Nano Energy* **68**, 104281 (2020).

33. Viegas, A., Mart, C. & Czernohorsky, M. Antiferroelectric Si:HfO_2 for High Energy Storage using 3D MIM Capacitors. In *2020 Joint Conference of the IEEE International Frequency Control Symposium and International Symposium on Applications of Ferroelectrics (IFCS-ISAF)*, 1–3 (IEEE, 2020).

34. Pech, D. *et al.* Ultrahigh-power micrometre-sized supercapacitors based on onion-like carbon. *Nature Nanotechnology* **5**, 651–654 (2010).

35. Huang, P. *et al.* On-chip and freestanding elastic carbon films for micro-supercapacitors. *Science* **351**, 691–695 (2016).

36. Zhang, P. *et al.* Zn-Ion Hybrid Micro-Supercapacitors with Ultrahigh Areal Energy Density and Long-Term Durability. *Advanced Materials* **31**, 1806005 (2019).

37. Xu, S. *et al.* Screen-printable microscale hybrid device based on MXene and layered double hydroxide electrodes for powering force sensors. *Nano Energy* **50**, 479–488 (2018).

38. Pech, D. *et al.* Elaboration of a microstructured inkjet-printed carbon electrochemical capacitor. *Journal of Power Sources* **195**, 1266–1269 (2010).

39. Dinh, T. M., Mesnilgrente, F., Conédéra, V., Kyeremateng, N. A. & Pech, D. Realization of an Asymmetric Interdigitated Electrochemical Micro-Capacitor Based on Carbon Nanotubes and Manganese Oxide. *Journal of The Electrochemical Society* **162**, A2016–A2020 (2015).

40. Létiche, M. *et al.* Sputtered Titanium Carbide Thick Film for High Areal Energy on Chip Carbon-Based Micro-Supercapacitors. *Advanced Functional Materials* **27**, 1606813 (2017).

41. Robert, K. *et al.* On Chip Interdigitated Micro-Supercapacitors Based on Sputtered Bifunctional Vanadium Nitride Thin Films with Finely Tuned Inter- and Intracolumnar Porosities. *Advanced Materials Technologies* **3**, 1800036 (2018).

42. Huang, P. *et al.* On-chip micro-supercapacitors for operation in a wide temperature range. *Electrochemistry Communications* **36**, 53–56 (2013).

43. Brousse, K. *et al.* Electrochemical behavior of high performance on-chip porous carbon films for micro-supercapacitors applications in organic electrolytes. *Journal of Power Sources* **328** (2016).

44. Li, L. *et al.* High-Performance Pseudocapacitive Microsupercapacitors from Laser-Induced Graphene. *Advanced Materials* **28**, 838–845 (2016).

45. Shen, C. *et al.* A high-energy-density micro supercapacitor of asymmetric MnO2–carbon configuration by using micro-fabrication technologies. *Journal of Power Sources* **234**, 302–309 (2013).

46. Hwang, J. Y. *et al.* Direct preparation and processing of graphene/RuO_2 nanocomposite electrodes for high-performance capacitive energy storage. *Nano Energy* **18**, 57–70 (2015).

47. Varzi, A., Bresser, D., von Zamory, J., Müller, F. & Passerini, S. $ZnFe_2O_4$-C/$LiFePO_4$-CNT: A Novel High-Power Lithium-Ion Battery with Excellent Cycling Performance. *Advanced Energy Materials* **4**, 1400054 (2014).

48. Wu, Z.-S. *et al.* Alternating Stacked Graphene-Conducting Polymer Compact Films with Ultrahigh Areal and Volumetric Capacitances for High-Energy Micro-Supercapacitors. *Advanced Materials* **27**, 4054–4061 (2015).

49. Shen, C., Wang, X., Zhang, W. & Kang, F. A high-performance three-dimensional micro supercapacitor based on self-supporting composite materials. *Journal of Power Sources* **196**, 10465–10471 (2011).

50. Shen, K., Ding, J. & Yang, S. 3D Printing Quasi-Solid-State Asymmetric Micro-Supercapacitors with Ultrahigh Areal Energy Density. *Advanced Energy Materials* **8**, 1800408 (2018).

51. Eustache, E. *et al.* High Areal Energy 3D-Interdigitated Micro-Supercapacitors in Aqueous and Ionic Liquid Electrolytes. *Advanced Materials Technologies* **2**, 1700126 (2017).

52. Dubal, D. P. *et al.* 3D hierarchical assembly of ultrathin MnO_2 nanoflakes on silicon nanowires for high performance micro-supercapacitors in Li-doped ionic liquid. *Scientific Reports* **5**, 9771 (2015).

53. Wang, X., Yin, Y., Li, X. & You, Z. Fabrication of a symmetric micro supercapacitor based on tubular ruthenium oxide on silicon 3D microstructures. *Journal of Power Sources* **252**, 64–72 (2014).

54. Beidaghi, M. & Wang, C. Micro-supercapacitors based on three dimensional interdigital polypyrrole/C-MEMS electrodes. *Electrochimica Acta* **56**, 9508–9514 (2011).

55. Durou, H. *et al.* Wafer-level fabrication process for fully encapsulated micro-supercapacitors with high specific energy. *Microsystem Technologies* **18**, 467–473 (2012).

56. Pu, J. *et al.* High-energy-density, all-solid-state microsupercapacitors with three-dimensional interdigital electrodes of carbon/polymer electrolyte composite. *Nanotechnology* **27**, 045701 (2016).

57. Dinh, T. M. *et al.* Hydrous RuO 2 /carbon nanowalls hierarchical structures for all-solid-state ultrahigh-energy-density micro-supercapacitors. *Nano Energy* **10**, 288–294 (2014).

58. Ferris, A., Garbarino, S., Guay, D. & Pech, D. 3D RuO_2 Microsupercapacitors with Remarkable Areal Energy. *Advanced Materials* **27**, 6625–6629 (2015).

59. Aradilla, D. *et al.* An innovative 3-D nanoforest heterostructure made of polypyrrole coated silicon nanotrees for new high performance hybrid micro-supercapacitors. *Journal of Materials Chemistry A* **3**, 13978–13985 (2015).

60. Su, Z. *et al.* Scalable fabrication of MnO_2 nanostructure deposited on free-standing Ni nanocone arrays for ultrathin, flexible, high-performance micro-supercapacitor. *Energy Environ. Sci.* **7**, 2652–2659 (2014).

61. Maeng, J., Kim, Y.-J., Meng, C. & Irazoqui, P. P. Three-Dimensional Microcavity Array Electrodes for High-Capacitance All-Solid-State Flexible Microsupercapacitors. *ACS Applied Materials & Interfaces* **8**, 13458–13465 (2016).

62. Alper, J. P. *et al.* Selective Ultrathin Carbon Sheath on Porous Silicon Nanowires: Materials for Extremely High Energy Density Planar Micro-Supercapacitors. *Nano Letters* **14**, 1843–1847 (2014).

63. El-Kady, M. F. *et al.* Engineering three-dimensional hybrid supercapacitors and microsupercapacitors for high-performance integrated energy storage. *Proceedings of the National Academy of Sciences* **112**, 4233–4238 (2015).

64. Kyeremateng, N. A., Brousse, T. & Pech, D. Microsupercapacitors as miniaturized energy-storage components for on-chip electronics. *Nature Nanotechnology* **12**, 7–15 (2017).

65. Zheng, S., Shi, X., Das, P., Wu, Z. & Bao, X. The Road Towards Planar Microbatteries and Micro-Supercapacitors: From 2D to 3D Device Geometries. *Advanced Materials* **31**, 1900583 (2019).

66. Cheema, S. S. *et al.* Emergent ferroelectricity in subnanometer binary oxide films on silicon. *Science* **376**, 648–652 (2022).

67. Park, J. Y. *et al.* Engineering Strategies in Emerging Fluorite-Structured Ferroelectrics. *ACS Applied Electronic Materials* **4**, 1369–1380 (2022).

68. Cheema, S. S. *et al.* Ultrathin ferroic HfO_2-ZrO_2 superlattice gate stack for advanced transistors. *Nature* **604**, 65–71 (2022).

69. Ali, T. *et al.* Impact of Stack Structure Control and Ferroelectric Material Optimization in Novel Laminate HSO and HZO MFMIS FeFET. In *2022 International Symposium on VLSI Technology, Systems and Applications (VLSI-TSA)*, 1–2 (IEEE, 2022).

70. Ali, T. *et al.* Tuning Hybrid Ferroelectric and Antiferroelectric Stacks for Low Power FeFET and FeRAM Applications by Using Laminated HSO and HZO films. *Adv. Electron. Mater.* **2100837**, 2100837 (2022).

71. Ni, K. *et al.* A Novel Ferroelectric Superlattice Based Multi-Level Cell Non-Volatile Memory. In *2019 IEEE International Electron Devices Meeting (IEDM)*, 28.8.1–28.8.4 (IEEE, 2019).

72. Ali, T. *et al.* A Multilevel FeFET Memory Device based on Laminated HSO and HZO Ferroelectric Layers for High-Density Storage. 28.7.1–28.7.4 (IEEE, 2019).

73. Schroeder, U., Park, M. H., Mikolajick, T. & Hwang, C. S. The fundamentals and applications of ferroelectric HfO_2. *Nature Reviews Materials* **7**, 653–669 (2022).

74. Kim, H. J. *et al.* Grain size engineering for ferroelectric $Hf_{0.5}Zr_{0.5}O_2$ films by an insertion of Al_2O_3 interlayer. *Applied Physics Letters* **105**, 192903 (2014).

75. Riedel, S., Polakowski, P. & Müller, J. A thermally robust and thickness independent ferroelectric phase in laminated hafnium zirconium oxide. *AIP Advances* **6**, 095123 (2016).

76. Mart, C., Kämpfe, T., Zybell, S. & Weinreich, W. Layer thickness scaling and wake-up effect of pyroelectric response in Si-doped HfO_2. *Applied Physics Letters* **112**, 052905 (2018).

77. Zheng, X.-q. *et al.* High Quality Factors in Superlattice Ferroelectric $Hf_{0.5}Zr_{0.5}O_2$ Nanoelectromechanical Resonators. *ACS Applied Materials & Interfaces* (2022).

78. Lederer, M. *et al.* Impact of the SiO_2 interface layer on the crystallographic texture of ferroelectric hafnium oxide. *Applied Physics Letters* **118**, 012901 (2021).

79. Lederer, M., Seidel, K., Olivo, R., Kämpfe, T. & Eng, L. M. Effect of Al_2O_3 interlayers on the microstructure and electrical response of ferroelectric doped HfO_2 thin films. *Frontiers in Nanotechnology* **4**, 1–8 (2022).

80. Lederer, M., Lehninger, D., Ali, T. & Kämpfe, T. Review on the microstructure of ferroelectric hafnium oxides. *physica status solidi (RRL) – Rapid Research Letters* 2200168 (2022).

81. Hyuk Park, M. *et al.* Evolution of phases and ferroelectric properties of thin $Hf_{0.5}Zr_{0.5}O_2$ films according to the thickness and annealing temperature. *Applied Physics Letters* **102**, 242905 (2013).

82. Starschich, S., Schenk, T., Schroeder, U. & Boettger, U. Ferroelectric and piezoelectric properties of $Hf_{1-x}Zr_xO_2$ and pure ZrO_2 films. *Applied Physics Letters* **110**, 182905 (2017).

83. Mimura, T., Shimizu, T. & Funakubo, H. Ferroelectricity in YO1.5-HfO_2 films around 1 μm in thickness. *Applied Physics Letters* **115**, 032901 (2019).

84. SHIMURA, R. *et al.* Preparation of near-1-μm-thick {100}-oriented epitaxial Y-doped HfO_2 ferroelectric films on (100)Si substrates by a radio-frequency magnetron sputtering method. *Journal of the Ceramic Society of Japan* **128**, 539–543 (2020).

85. Schenk, T. *et al.* Toward Thick Piezoelectric HfO_2-Based Films. *physica status solidi (RRL) – Rapid Research Letters* **14**, 1900626 (2020).

86. Shimura, R. *et al.* No-Heating Deposition of 1-μm-Thick Y-Doped HfO_2 Ferroelectric Films with Good Ferroelectric and Piezoelectric Properties by Radio Frequency Magnetron Sputtering Method. *physica status solidi (RRL) – Rapid Research Letters* **2100574**, 2100574 (2022).

87. Garvie, R. C. The occurrence of metastable tetragonal zirconia as a crystallite size effect. *Journal of Physical Chemistry* **69**, 1238–1243 (1965).

88. Pitcher, M. W. *et al.* Energy crossovers in nanocrystalline zirconia. *Journal of the American Ceramic Society* **88**, 160–167 (2005).

89. Shandalov, M. & McIntyre, P. C. Size-dependent polymorphism in HfO_2 nanotubes and nanoscale thin films. *Journal of Applied Physics* **106**, 0–5 (2009).

90. Gerson, R. & Marshall, T. C. Dielectric Breakdown of Porous Ceramics. *Journal of Applied Physics* **30**, 1650–1653 (1959).

91. Neusel, C. *et al.* Thickness-dependence of the breakdown strength: Analysis of the dielectric and mechanical failure. *Journal of the European Ceramic Society* **35**, 113–123 (2015).

92. Yang, L. *et al.* Perovskite lead-free dielectrics for energy storage applications. *Progress in Materials Science* **102**, 72–108 (2019).

93. Mise, N. *et al.* Scalability of TiN/HfAlO/TiN MIM DRAM capacitor to 0.7-nm-EOT and beyond. In *2009 IEEE International Electron Devices Meeting (IEDM)*, 1–4 (I EEE, 2009).

94. Kim, Y., Min, K. K., Yu, J., Kwon, D. & Park, B.-G. Lamination method for improved polarization-leakage current relation in HfO_2-based metal/ferroelectric/insulator/semiconductor structure. *Semiconductor Science and Technology* **37**, 045001 (2022).

95. Khan, A. I. *et al.* Negative capacitance in a ferroelectric capacitor. *Nature Materials* **14**, 182–186 (2015).

96. Khan, A. I. *et al.* Experimental evidence of ferroelectric negative capacitance in nanoscale heterostructures. *Applied Physics Letters* **99**, 113501 (2011).

97. Hoffmann, M. *et al.* Antiferroelectric negative capacitance from a structural phase transition in zirconia. *Nature Communications* **13**, 1228 (2022).

98. Qiao, L. *et al.* Observation of negative capacitance in antiferroelectric $PbZrO_3$ Films. *Nature Communications* **12**, 4215 (2021).

99. McPherson, J., Kim, J., Shanware, A., Mogul, H. & Rodriguez, J. Proposed universal relationship between dielectric breakdown and dielectric constant. In *Digest. International Electron Devices Meeting,*, 633–636 (IEEE, 2002).

100. McPherson, J., Jinyoung Kim, Shanware, A., Mogul, H. & Rodriguez, J. Trends in the ultimate breakdown strength of high dielectric-constant materials. *IEEE Transactions on Electron Devices* **50**, 1771–1778 (2003).

101. McPherson, J., Kim, J.-Y., Shanware, A. & Mogul, H. Thermochemical description of dielectric breakdown in high dielectric constant materials. *Applied Physics Letters* **82**, 2121–2123 (2003).

102. Kim, J. *et al.* Ultrahigh capacitive energy density in ion-bombarded relaxor ferroelectric films. *Science* **369**, 81–84 (2020).

103. Miller, J. R. & Simon, P. Electrochemical Capacitors for Energy Management. *Science* **321**, 651–652 (2008).

104. Kim, H. J. *et al.* Low-Thermal Budget Fluorite-Structure Ferroelectrics for Future Electronic Device Applications. *physica status solidi (RRL) – Rapid Research Letters* **15**, 2100028 (2021).

105. Shelimov, K. B., Davydov, D. N. & Moskovits, M. Template-grown high-density nanocapacitor arrays. *Applied Physics Letters* **77**, 1722–1724 (2000).

106. Sohn, J. I. *et al.* Fabrication of high-density arrays of individually isolated nanocapacitors using anodic aluminum oxide templates and carbon nanotubes. *Applied Physics Letters* **87**, 123115 (2005).

107. Roozeboom, F., Elfrink, R., Verhoeven, J., van den Meerakher, J. & Holthuysen, F. High-value MOS capacitor arrays in ultradeep trenches in silicon. *Microelectronic Engineering* **53**, 581–584 (2000).

108. Gogotsi, Y. & Simon, P. True Performance Metrics in Electrochemical Energy Storage. *Science* **334**, 917–918 (2011).

109. Aricò, A. S., Bruce, P., Scrosati, B., Tarascon, J.-M. & van Schalkwijk, W. Nanostructured materials for advanced energy conversion and storage devices. *Nature Materials* **4**, 366–377 (2005).

110. Kemell, M. *et al.* Si/Al_2O_3/ZnO:Al capacitor arrays formed in electrochemically etched porous Si by atomic layer deposition. *Microelectronic Engineering* **84**, 313–318 (2007).

111. Sherrill, S. A., Banerjee, P., Rubloff, G. W. & Lee, S. B. High to ultra-high power electrical energy storage. *Physical Chemistry Chemical Physics* **13**, 20714–20723 (2011).

112. Polakowski, P. *et al.* Ferroelectric deep trench capacitors based on Al:HfO2 for 3D non-volatile memory applications. In *2014 IEEE 6th International Memory Workshop (IMW)*, 1–4 (IEEE, 2014).

113. Laïk, B., Ressejac, I., Venet, C. & Pereira-Ramos, J. P. Comparative study of electrochemical performance of commercial solid-state thin film Li microbatteries. *Thin Solid Films* **649**, 69–74 (2018).

114. Materials, methods, and additional information are available as supplementary materials. .

115. Lethien, C., Le Bideau, J. & Brousse, T. Challenges and prospects of 3D micro-supercapacitors for powering the internet of things. *Energy & Environmental Science* **12**, 96–115 (2019).

116. Xia, Q. *et al.* All-Solid-State Thin Film Lithium/Lithium-Ion Microbatteries for Powering the Internet of Things. *Advanced Materials* **7**, 2200538 (2022).

117. Simon, P. & Gogotsi, Y. Perspectives for electrochemical capacitors and related devices. *Nature Materials* **19**, 1151–1163 (2020).

118. Gargini, P., Balestra, F. & Hayashi, Y. Roadmapping of Nanoelectronics for the New Electronics Industry. *Applied Sciences* **12**, 308 (2021).

119. Famprikis, T., Canepa, P., Dawson, J. A., Islam, M. S. & Masquelier, C. Fundamentals of inorganic solid-state electrolytes for batteries. *Nature Materials* **18**, 1278–1291 (2019).

120. Zhao, Q., Stalin, S., Zhao, C.-Z. & Archer, L. A. Designing solid-state electrolytes for safe, energy-dense batteries. *Nature Reviews Materials* **5**, 229–252 (2020).

121. Oudenhoven, J. F. M., Baggetto, L. & Notten, P. H. L. All-Solid-State Lithium-Ion Microbatteries: A Review of Various Three-Dimensional Concepts. *Advanced Energy Materials* **1**, 10–33 (2011).

122. Salanne, M. *et al.* Efficient storage mechanisms for building better supercapacitors. *Nature Energy* **1**, 16070 (2016).

123. Randau, S. *et al.* Benchmarking the performance of all-solid-state lithium batteries. *Nature Energy* **5**, 259–270 (2020).

124. Zhu, Y. *et al.* Lithium-film ceramics for solid-state lithionic devices. *Nature Reviews Materials* **6**, 313–331 (2020).

125. Tan, D. H. S., Banerjee, A., Chen, Z. & Meng, Y. S. From nanoscale interface characterization to sustainable energy storage using all-solid-state batteries. *Nature Nanotechnology* **15**, 170–180 (2020).

126. Kim, K. J., Balaish, M., Wadaguchi, M., Kong, L. & Rupp, J. L. M. Solid-State Li–Metal Batteries: Challenges and Horizons of Oxide and Sulfide Solid Electrolytes and Their Interfaces. *Advanced Energy Materials* **11**, 2002689 (2021).

127. Mart, C. *et al.* Energy Harvesting in the Back-End of Line with CMOS Compatible Ferroelectric Hafnium Oxide. In *2020 IEEE International Electron Devices Meeting (IEDM)*, 26.3.1–26.3.4 (IEEE, 2020).

128. Lheritier, P. *et al.* Large harvested energy with non-linear pyroelectric modules. *Nature* 10.1038/s41586–022–05069–2 (2022).

129. Park, D.-S. *et al.* Induced giant piezoelectricity in centrosymmetric oxides. *Science* **375**, 653–657 (2022).

130. Zhang, H. *et al.* Atomically engineered interfaces yield extraordinary electrostriction. *Nature* **609**, 695–700 (2022).

131. Keshavarzi, A. & van den Hoek, W. Edge Intelligence—On the Challenging Road to a Trillion Smart Connected IoT Devices. *IEEE Design & Test* **36**, 41–64 (2019).

132. Keshavarzi, A., Ni, K., Van Den Hoek, W., Datta, S. & Raychowdhury, A. FerroElectronics for Edge Intelligence. *IEEE Micro* **40**, 33–48 (2020).

133. Zhu, M. & Schmidt, O. G. Tiny robots and sensors need tiny batteries — here's how to do it. *Nature* **589**, 195–197 (2021).

134. Aubin, C. A. *et al.* Towards enduring autonomous robots via embodied energy. *Nature* **602**, 393–402 (2022).

135. Liang, Z. *et al.* Next-Generation Energy Harvesting and Storage Technologies for Robots Across All Scales. *Advanced Intelligent Systems* 2200045 (2022).

136. Stauth, J. T. Pathways to mm-scale DC-DC converters: Trends, opportunities, and limitations. *2018 IEEE Custom Integrated Circuits Conference, CICC 2018* 1–8 (2018).